Tamminen, Aleksi; Palli, Samu Ville; Ala-Laurinaho, Juha; Salkola, Mika; Räisänen, Antti; Taylor, Zachary

Quasioptical System for Corneal Sensing at 220-330 GHz

Published in:
IEEE Transactions on Terahertz Science and Technology

DOI:
10.1109/TTHZ.2020.3039454

Published: 01/03/2021

Document Version
Peer-reviewed accepted author manuscript, also known as Final accepted manuscript or Post-print

Please cite the original version:
Tamminen, A., Palli, S. V., Ala-Laurinaho, J., Salkola, M., Räisänen, A., & Taylor, Z. (2021). Quasioptical System for Corneal Sensing at 220-330 GHz: Design, Evaluation, and Ex Vivo Cornea Parameter Extraction. *IEEE Transactions on Terahertz Science and Technology*, *11*(2), 135 - 149. Article 9264654. https://doi.org/10.1109/TTHZ.2020.3039454

Quasioptical system for corneal sensing at 220 - 330 GHz: design, evaluation, and *ex-vivo* cornea parameter extraction

A. Tamminen, S.-V. Pälli, J. Ala-Laurinaho, M. Salkola, A. V. Räisänen, and Z. D. Taylor

Abstract*— The design, simulation, and characterization of a quasioptical system for submillimeter-wave quantification of corneal thickness and water content are presented. The optics operate in the 220-330 GHz band and are comprised of two, custom aspheric, biconvex lenses in a gaussian beam telescope configuration. The design produces broad band wavefront curvature matching to 7.5 mm radius of curvature target surfaces thus emulating a plane-wave-on-planar-media condition and enabling application of stratified medium theory to data analysis. Aspheric lens coefficients were optimized with geometric ray tracing subject to optical path length penalties and physical optics simulations showed aspheric designs achieved wavefront coupling to spherical surfaces, superior to equivalent, canonical hyperbolic lenses. The fabricated lens system was characterized in a planar near-field scanner system and demonstrated good agreement to physical-optics simulations. An average central corneal thickness of 652 μm and free water content volume of 47 % were extracted from *ex vivo* sheep corneas via complex s-parameters and agree with literature values. Extracted contact lens thickness and water content agreed with independently validated values. Moreover, the quasioptical system enabled observation of dynamic changes in artificial tear-film, thickness, and water content. This work elucidates two major findings related to submillimeter-wave wavefront matching on spherical surfaces, with wavelength order radii of curvature: (1) An asphere whose sag coefficients are optimized via field phase variation on a spherical surface produces coupling superior to a plano-hyperbolic lens. (2) For most feasible apertures, the Gaussian beam waist is located in the aperture near field, suggesting consideration for operating in the beam near field.

***Index Terms*— Cornea, millimeter waves, quasioptics.**

I. Introduction

The exploration of submillimeter-wave based sensing in biomedical applications is an active area of research. Changes in tissue water content (TWC) are often considered an indication of abnormality stemming from disease or injury [1], [2]. Millimeter-wave reflectivity measurements for corneal characterization have been carried out in [1]-[5].

Manuscript received March 25, 2020; revised September 25, 2020; accepted November 4, 2020. This work has been funded through Revenio Oy and research project AGRUM of Academy of Finland programme Radiation Detectors for Health, Safety and Security (RADDESS). A. Tamminen, S.-V. Pälli, J. Ala-Laurinaho, A. V. Räisänen, and Z. D. Taylor are with Aalto University Department of Electronics and Nanoengineering, MilliLab, Espoo, Finland (phone: +358505137989, email: aleksi.tamminen@aalto.fi). M. Salkola is with Revenio Oy, Vantaa, Finland.

Millimeter waves are especially suitable for corneal-tissue characterization as the tissue is very homogenous in the considered wavelength range and it consists of two main constituents; collagen and water. The constituents and their relative concentration, corneal-tissue water content (CTWC), can be modeled with the mixed medium theory such as Bruggeman's model [6], [7]. The millimeter-wave reflectivity of cornea is a strong function of its water content. Furthermore, the cornea is nearly spherical at sub-millimeter-wavelength scale making it especially suitable for efficient coupling to a Gaussian beam [8]. A natural design rule is to achieve a broadband match between the output wave front and the corneal surface. Previous work has hypothesized that the corneal central thickness (CCT) and CTWC can be extracted from the measured broadband reflection coefficient. This approach related submillimeter-wave a and THz reflectivity to CCT and CTWC via a model based on stratified medium theory and effective media theory. However, this model assumed infinite transverse extent, planar layers and normal incidence plane wave illumination with [2], [9]. However, the focused Gaussian-beam illumination and layered, concentric spherical shells (cornea) present geometry where plane wave conditions can only be approximated. The back-reflected field may be represented by stratified medium theory depending on the match between Gaussian beam phase front and corneal radius of curvature. There is limited detail in the existing literature discussing the alignment issues between the cornea or corneal phantom geometry and Gaussian beam at (sub)millimeter waves although Gaussian beam incident on spherical surfaces have been studied at optical wavelengths (e.g. [10], [11]).

Tight focusing of THz beams with aspheric, dielectric lenses, and associated near-field effects have been studied in [12]. In previous work describing quasioptical designs for corneal sensing, the curved surface is typically illuminated so that the Gaussian-beam waist is placed at the corneal (phantom) center of curvature (CoC) [5], [8]. However, at (sub)millimeter waves the corneal radius of curvature is of the order of the Gaussian-beam waist and wavelength, which inherently affects the optimal alignment and limits the bandwidth. Optimal coupling suggests the Gaussian-beam radius of curvature (RoC) match the cornea RoC (~ 7.5 mm), which typically leads to a virtual sub-wavelength Gaussian-beam waist significantly displaced from the corneal CoC. Often, a broadband THz system is coupled to the sample with two groups of mirrors [5] or lenses [1], [13]: one group delivering the transmitted waves to the sample and the second group directing the reflected waves to the detector. Because of the separate groups of focusing elements, the incident angle is not always parallel with the corneal optical axis. Additionally, the illumination electric field direction of propagation is not always parallel to local surface normal; especially in case of curved samples. This limits the utility of stratified medium theory applied to plane wave illumination in measurement analysis, unless the added complexity is considered.

In addition to optimal positioning between the sample and Gaussian beam, the practical realization of quasioptics affects the coupling to and from the cornea sample. To enhance correlation with CCT measurements, it is beneficial that the incident beam illuminates an area confined to the corneal center. CCT increases monotonically towards the periphery and significant reflection from there could lead to misinterpretation of the central corneal thickness [14]. To interrogate the central cornea, the Gaussian beam radius on the corneal surface should limited to a few millimeters. Smaller illumination spot radii are possible but may impede a broad band radius of curvature match. Moreover, it is important to minimize the frequency dependency of the output beam at the corneal surface. For example, the phase-center location and the transverse extent should be constant to maximize the compatibility of stratified medium theory-based analysis across a sufficient measurement bandwidth.

To address these design challenges, a Gaussian-beam telescope with customized bi-convex, aspheric refracting elements is realized for the 220-330 GHz band. A compact ABCD matrix description of aligning a spherical surface to a converging Gaussian beam is given in Section II. Physical-optics simulations of a Gaussian beam are presented Section III and elucidate design challenges associated with broad-band phase front matching. Section IV presents the phase-coherent raytracing-based design of the quasioptics. We continue with more accurate PO simulations in Section V by comparing the optimized aspheric design with a pair of canonical hyperbolic lenses. Experimental characterization of the manufactured aspheric lens quasioptics is discussed in Section VI and the first results with a cornea phantom and *ex vivo* sheep corneas in Section VII. Section VIII discusses the spherical sample in the near field of the lens aperture and details future directions.

II. Analysis of Gaussian Beams Incident on Curved Surfaces

Nominal, theoretical corneal reflectivity is shown in Fig. 1. The reflected magnitude and phase are computed with the stratified media and effective media theory described in [15] with the absence of a thickness dimension gradient, while assuming free water content of 60 % and relative permittivity of collagen and bound water of 2.9. The corneal central thickness was 500 μm, falls within values reported in the literature [14]. The 60 % free-water content assumes about 20 % bound water with a relative bound water dielectric permittivity of 2.9 based on values reported in [7], [16], and [17]. Free-water dielectric permittivity was modeled with double-Debye relaxation. Fig. 1 shows the reflection calculated for the nominal cornea as well superimposed on curves for increased thickness (ΔCCT) and water content (ΔCTWC). The free-water dielectric loss results in exponential, asymptotic envelopes for the magnitude and phase. At low frequency, the interfering reflections from the anterior and posterior cornea manifest as significant oscillations in the frequency domain. As the loss per unit length increases at higher frequency, the oscillations are damped. At high frequency, the magnitude and phase trend towards the reflectivity expected form a lossy half space.

While subject to more accurate analysis, Fig. 1 shows that the changes in corneal parameters can be extracted if the interfering reflections due to thickness and decay can be decoupled with reasonable SNR as well as it demonstrates the utility of increasing bandwidth. However, suitable Gaussian-beam parameters that maintain plane-wave like conditions on the cornea (locally normal incidence across the curved field of view) are difficult to maintain over large bandwidth. Furthermore, achieving sufficient beam parameters are especially difficult below 150 GHz, where the most prominent spectral features lie but where the wavelength is a significant fraction of the corneal-geometry dimensions (radius of curvature, *en face* diameter). The first rectangular waveguide band spanning over the roughly 100-GHz period of the spectral features is WR-3.4 and thus was selected as the operating band for the presented quasioptics. At this band, the modeled reflectivity from cornea varies of the order of 1 % in amplitude and 1° in phase upon realistic change in corneal parameters (Fig. 1).

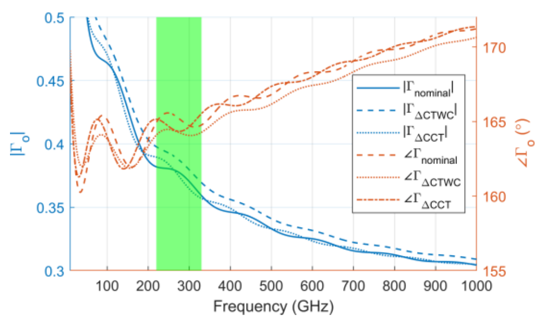

Fig. 1. Theoretical reflectivity for a typical cornea. Three variations are shown: Nominal cornea (solid), increase in water content (ΔCTWC = 6 %, dashed), and increase in thickness (ΔCCT = 60 μm, dotted). The shaded area shows the selected WR-3.4 waveguide band the analysis is based on in this work.

This analysis is restricted to fundamental-mode Gaussian beams (TEM_{00}) with the following characteristic parameters: beam waist radius (w_0), axially-varying beam radius (w), and axially-varying beam radius of curvature (R) [18]. The functional dependence of R, w, and w_0 on z is omitted here but it is expressed in the succeeding text for clarity. As discussed previously [5], optimal positioning of the illumination beam with respect to the corneal surface is defined as the approximate equality of beam radius of curvature $R(z)$ and corneal radius of curvature R_s: $R(z) \approx R_s$. The radii of curvature of the cornea and of a Gaussian beam are equal on axis at two locations:

$$z_{\pm} = \frac{R_s \pm \sqrt{{R_s}^2 - 4{z_c}^2}}{2}. \quad (1)$$

The corneal radius of curvature (R_s) is on the order of the confocal distance ($z_c = \pi {w_0}^2/\lambda$) for the WR-3.4 band and as a result, the alignment to cornea is strongly influenced by quasioptical element focal lengths, illumination bandwidth, and aperture diameters.

Three locations are relevant for coupling a Gaussian beam to aspherical surfaces: at the two solutions to Equation (1), and a third orientation where the corneal apex is coincident with the beam waist. Illuminating the cornea with the beam waist does not produce a curvature match but it's study was motivated results presented in the literature where separate transmitter and receiver paths are coupled through corneal surface at the collocating foci of beams [13], [18]-[20].

The solutions to equation (1) are labeled "superconfocal distance" and "subconfocal distance", z_+ and z_- as roots, respectively. Fig. 2 demonstrates the cases where the spherical cornea anterior surface is located in the Gaussian beam at superconfocal, subconfocal, and waist distances at 275 GHz computed with a waist radius of $w_0 = 0.8\lambda_0$. The Gaussian-beam wavefront approximates the spherical surface at the super- and subconfocal distances. Due to $z_c \approx R_s$, the match deteriorates (1) as the frequency deviates from midband and (2) as the beam parameters vary around the vicinity of the beam waist. The approximation at the waist location is always non-optimal due to the planar wave front of the waist. Note that the Gaussian beam phase front is not perfectly spherical and the match deviates for points off-axis, as indicated in the insets in Fig. 2. The deviation from a sphere increases radially. Compared to traditional quasioptical designs, where any characteristic dimension in a setup may be tens or hundreds of wavelengths, here the interaction with the Gaussian beam occurs within about ten free-space wavelengths dimension and thus beam parameters vary greatly with frequency. In such a quasioptics, the distance to radiating aperture is typically less than the Fresnel region distance and the near-field effects affect the quality of the converging Gaussian beam to a significant extent [21] (this feature constraint is further discussed in Section V).

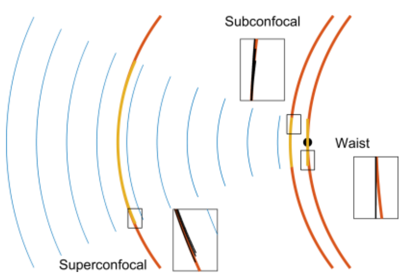

Fig. 2. Gaussian beam incident on a spherical surface. At midband, the radius of curvature of the beam matches with that of the surface at super- and subconfocal distances. At other frequencies the matching reduces (black lines in insets).

Equation (1) and Fig. 2 suggest that the confocal distance, z_c, and the waist location should be frequency invariant for broad-band operation. Additionally, Equation (1) provides an upper bound on confocal distance:

$$z_c \leq R_s/2. \quad (2)$$

For a corneal surface $R_s = 7.5$ mm, this results in maximum Gaussian-beam waist of 1.04-1.27 mm at WR-3.4 band of 220 GHz - 330 GHz. A summary of the operating points are displayed in Fig. 3 which shows the axial dependent RoC of three different, converging gaussian beams with waist located at $z = 0$. The beams were parameterized by beam waist w_0 and computed for a frequency of 275 GHz. The $R(z) = R_s$ and $z = R_s$ lines are indicated.

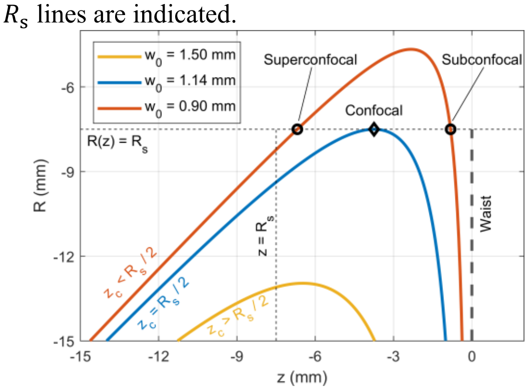

Fig. 3. Converging beam radius of curvature showing three different operating points for coupling: superconfocal, subconfocal, and waist.

The curve labeled $z_c < R_s/2$ describes a beam with waist radius $w_0 = 0.9$ mm whose RoC, $R(z)$, at the confocal distance z_c is smaller than R_s: $|R(z = z_c)| < |R_s|$. This parameterization results in two intersections between $R(z)$ and R_s labeled "superconfocal" and "subconfocal", respectively. The curve labeled $z_c = R_s/2$ describes a beam with waist radius 1.14 mm whose RoC at the confocal distance is equal to R_s: $|R(z = z_c)| = |R_s|$ resulting in only one intersection point labeled "Confocal". The $w_0 = 1.50$ mm parameterization is labeled $z_c > R_s/2$ and produces a beam whose RoC never reaches R_s: $|R(z = z_c)| > |R_s|$.

III. Physical Optics Simulations of a Realistic Beam on Target

The optimal locations given by Equation (1) consider wave-front matching only on the axis of propagation. For more accurate alignment and analysis of bandwidth, the Gaussian beam incident on cornea is simulated with an in-house developed physical-optics (PO) code. The method follows the formalism of calculating the electric and magnetic fields outside radiating apertures [15],[22]. Both electric and magnetic fields were calculated to determine the local Poynting vector and thus direction of wave propagation. The incidence angle on the corneal surface was calculated as

$$\theta_i = \cos^{-1}\frac{\mathbf{n}\cdot\mathbf{S}}{|\mathbf{n}||\mathbf{S}|}, \quad (3)$$

where $\mathbf{n}$ is the surface normal and $\mathbf{S} = \mathbf{E}\times\mathbf{H}$ is the Poynting vector. The electric field coupling coefficient was used for estimating coupling between the incident Gaussian beam and back-reflected beam

$$c_a = \frac{\sum E_a E_b}{\sum E_a E_a^*}, \quad (4)$$

where E_a is the electric field emanating from the reference plane and E_b is the electric field returning to the reference plane following scattering from the spherical target surface.

A. Aligning sample with Gaussian beam

PO simulations were performed with a physically realizable confocal distance informed by the measured beam pattern data from the Gaussian-beam telescope presented in this work. The confocal distance is conservatively about half the maximum confocal distance given by Equation (2). Due to the slightly different E- and H-plane beam feedhorn beam widths and polarization effects arising from the quasioptics, the output beam was astigmatic and the confocal distance was determined separately for the two planes; ~ 2.4 mm for E-plane and ~ 2.1 mm for H-plane. When applying to Equation (1), the subconfocal distances are $z_{-} \approx 0.82$ mm and 0.64 mm, whereas the superconfocal distances are $z_{+} \approx 6.68$ mm and 6.86 mm in E- and H-planes, respectively. Initial simulations addressed an ideal TEM00 Gaussian beam emanating from an aperture, reflecting from curved surface, and returning to the aperture to assess an upper bound on matching. Simulations of including lenses are discussed in Section V. A diagram description of the simulation setup is shown in Fig. 4 for example axial offsets $z = 0$ mm, 0.82 mm, 6.68 mm and 7.5 mm (R_s).

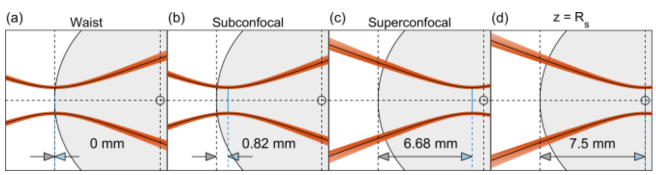

Fig. 4. Ensemble of ideal gaussian beam over the 220 GHz – 330 GHz band with frequency invariant confocal distance $z_c = 2.4$ mm and collocated beam waist locations. The beams are superimposed on a 7.5 mm RoC sphere and (a) – (d) are parameterized by offset between corneal apex and waist.

Fig. 5 shows the PO simulation of the electric field coupling coefficient from 220-330 GHz for a spherical conductor surface at varying positions with respect to the corneal apex, along the optical axis. The coupling coefficient is, on average maximized, at the ensemble averaged subconfocal distance $z_{-} \approx 0.85$ mm and superconfocal distance $z_{+} \approx 6.75$ mm, with peak-to-peak variation of 0.25 mm at both distances. Coupling coefficients are relatively constant at the optimal positions and varies more elsewhere as function of frequency. The superconfocal distance peak is slightly higher than subconfocal distance peak.

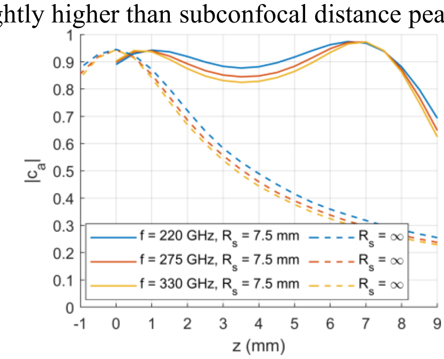

Fig. 5. Simulated field-coupling coefficient for the reflection from a spherical (solid) target at 220-330 GHz. The high coupling coefficient observed at waist, subconfocal distance, and superconfocal position indicate good matching between sample surface and incoming wave front. For comparison, also the reflection from a flat target is shown (dashed).

The peak locations identified by PO simulation differ from Equation (1) due to the PO simulation capturing the whole surface as opposed to ABCD matrix analysis which considers just the on axis field. Both the analytic and simulated distances corresponding to peak coupling coefficient differ critically from examples in literature, where the corneal surface is often positioned at $z = 0$ mm (Fig. 4 a) or $z = R_s$ (Fig. 4 d).

B. Incidence angle on the cornea

Current methods to extract corneal water content and its decoupling from corneal thickness are reliant on plane-wave analysis and stratified-medium theory. Electric and magnetic fields computed with the PO simulation enabled estimates of local incidence angles between the Gaussian beam wave front and corneal surface. Fig. 6 shows the incidence angle and normalized electric field when the corneal apex is positioned at the beam waist, subconfocal position, and superconfocal position. The closer to the beam waist location, the faster the incidence angle increases when moving away from the optical axis. Within a normalized $1/e^2$ radius, the average incidence angle is 5.7°, 2.5°, and 1.0° for the waist, subconfocal, and superconfocal positions, respectively.

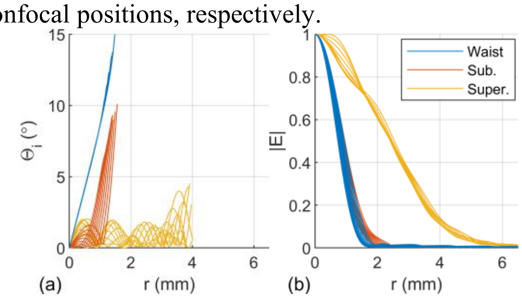

Fig. 6. Simulated a) incidence angle and b) normalized amplitude on curved surface for different surface positions at 220-330 GHz. The incidence angle is drawn down to normalized amplitude of $1/e^2$.

These results indicate that a significant fraction of the incident field undergoes oblique reflection with increasing fraction for decreasing distance to the beam waist. Increasing incidence angle limits the utility of planar, stratified media based analysis as spatially varying incidence angles dampen the constructive/destructive interference of fields reflected by different corneal layers.

C. Predicted corneal reflection coefficient

The observed reflection coefficient was obtained by normalizing the reflection from cornea with that from a PEC surface with the same radius of curvature:

$$\Gamma_o = -\frac{c_{a,c}}{c_{a,PEC}}, \tag{5}$$

where $c_{a,c}$ and $c_{a,PEC}$ are the coupling coefficients. Normalization eliminates the effect of free-space propagation to and from the curved surface. Fig. 7 shows the predicted reflection coefficient at the aforementioned positions with comparison to the theoretical reflection coefficient from the stratified medium theory. Each point on the cornea was treated as locally infinite with an incident plane wave in the PO simulation. The estimation does not consider the walk-off phenomena that will occur with a converging beam inside the cornea, which reduce the accuracy to some extent. Fig. 7 shows the predicted reflection coefficient also in the case of 0.2-mm difference in the radius of curvature. The error between computation and the theoretical reflection coefficient is small for all positions where the normalization is done in equal geometries: Peak-to-peak amplitude error is 0.06 % and peak-to-peak phase error is 0.024°. For the case of slightly different geometries in cornea and normalization surface, the error increases and is significantly different for different positions of the surface: Mean amplitude and phase error is maximized at superconfocal position: −0.38 % and 4.72°.

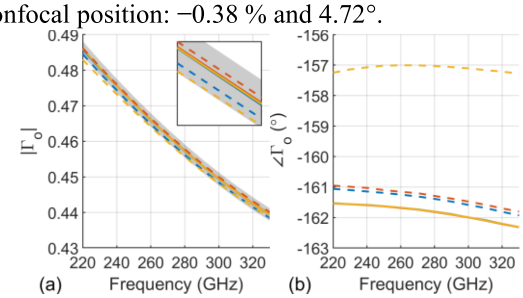

Fig. 7. Simulated observed reflection coefficient nominal cornea. Simulations are run for cornea at waist (blue), sub- (red), and superconfocal (yellow), positions. Dashed lines show normalization with 0.2-mm geometry error. Theoretical reflection coefficient range for $CTWC = 78 \pm 1\%$ is shown with dark shade.

D. *Effect of radially dependent corneal thickness*

Human cornea is nominally 400 µm - 700 µm thick with an anterior radius of curvature of 7.8 mm and posterior radius of curvature of 6.4 mm [23]. This geometry results in an increasing corneal thickness as a function of radius from the optical axis. As the cornea is illuminated over an appreciable *en face* radius, parts of the cornea with different thicknesses contribute to the aggregate observed millimeter-wave reflectivity. The observed reflectivity can be approximated as

$$\Gamma_{\mathrm{o}} \approx \frac{\sum \rho(f, r_i) E_{\mathrm{i}}}{\sum E_{\mathrm{i}}}, \tag{6}$$

where $\rho(f, r_i)$ is the reflection coefficient of the cornea, E_{i} is the incident electric field, f is illumination frequency, and r_i the radius from the optical axis. Fig. 8 investigates a scenario, where constant electric field and perpendicular incidence angle is considered.

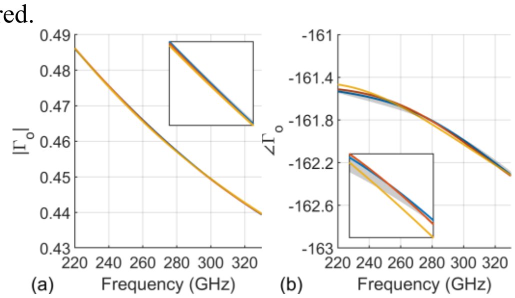

Fig. 8. Observed reflectivity a) amplitude and b) phase for typical cornea for different maximum radius of the beam: Only vertex of the cornea considered (blue), beam extends to radius of 2 mm (red), and 4 mm (yellow). Theoretical reflection coefficient range for $CTWC = 78 \pm 1\%$ is shown with dark shade.

The observed reflection coefficient varies as the beam covers further parts of the corneal surface. At maximum, the peak-to-peak phase error is up to 0.11°. At 2-mm en-face radius, the peak-to-peak phase error is 0.04°. While it is difficult to judge the tolerable error in observed reflection coefficient, clearly it is beneficial to illuminate the cornea centrally to arrive to a clinically relevant estimate of the CCT. To achieve that, a beam with high Gaussicity is preferred. To limit the effect of increasing corneal thickness, it is beneficial to align cornea at subconfocal distance. For comparison, commercial ultrasonic pachymeter (PachPen, Accutome Inc.) has sensor diameter of 2.5 mm for probing the cornea.

IV. Quasioptical Design

The above analysis is based on analytical Gaussian-beam theory and PO simulations of the fundamental mode beam. The analysis suggests design rules for practical quasioptics coupling to curved surfaces:

1. The confocal distance of the output beam should be invariant and at maximum half of the sample radius of curvature across the band.
2. The Gaussian output beam must be aligned so that the curved surface collocates with the wave front at positions given approximately by Equation (1).
3. The normalization used in the measurement is sensitive to the differences in geometries especially when the sample is placed further away from the confocal distance.
4. The spot size on cornea should be constrained to limit the effect of radial cornea thickness variation to observed reflection coefficient.

The preceding analysis showed that design point 2 indicates superconfocal operation while design point 4 favors subconfocal operation.

A. *Gaussian-beam telescope*

The Gaussian-beam telescope configuration uses a pair of focusing elements separated by the sum of their focal lengths. This produces a frequency-invariant output waist location and output waist radius of

$$w_{0,\mathrm{out}} = \frac{f_2}{f_1} w_{0,\mathrm{in}}, \tag{7}$$

where $w_{0,\mathrm{in}}$ is the input beam waist and f_1 and f_2 are the focal lengths of optic 1 and 2 [18]. The quasioptical system feed was a corrugated horn antenna optimized at 310 GHz with an expected frequency-dependent beam waist size and location and thus a frequency-dependent output beam waist follows. In this case, the frequency dependency of the beam waist results in relatively constant confocal distance across the band, which fulfils the design rules 1-4 described above. A sketch of the millimeter-wave measurement system is shown in Fig. 9. The Gaussian beam from the transceiver is collimated by the first aspheric biconvex lens and the second aspheric biconvex lens focuses the beam on the curved sample.

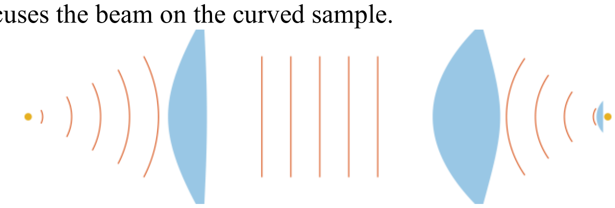

Fig. 9. Sketch of the quasioptics based on two bi-convex aspheric lenses. Dots show the locations of the focal points. Corneal surface is located before the second focus on the right side of the figure.

A general aspheric surface is defined by the standard sag equation:

$$z_a(s) = \frac{cs^2}{1+\sqrt{1-(1+k)cs^2}} + \sum_i A_i s^{2i} + t_l, \quad (8)$$

where s is the radius from optical axis, c is the curvature, k is conic constant, A_i is the i^{th} higher order coefficient, and t_l is the position of the surface vertex on the z-axis [24]. To justify a customized aspheric lens design, the simulated performance was compared to the canonical hyperbolic plano-convex lenses. A hyperbolic surface is defined as

$$z_h(s) = \frac{f}{n+1}\left(\sqrt{1+\frac{(n+1)s^2}{(n-1)f^2}}-1\right), \quad (9)$$

where f is the focal length of the surface and n is the refractive index of the medium [18]. The goal of the second optic in the gaussian beam telescope is to interrogate the cornea by creating frequency invariant, spherical, converging phase front from a collimated input beam centered around and parallel to the optical axis. In geometric optics, a spherical phase front implies a focused point source with minimal aberration at the focal plane. This points to the hyperbolic plano-convex surface as the optimal element. However, aspheric surfaces allow more degrees of freedom on spatial optimization of the field on cornea outside the geometric focus.

The lens material was cyclic-olefin copolymer, TOPAS 6013S-04 from Nordbergs Tekniska AB, Sweden. The material has low loss at submillimeter waves and mechanical properties suitable for CNC machining. The relative dielectric permittivity was at 500 GHz is ~ 2.32−j0.001 [25] and this same value was used for simulations at 220-330 GHz.

The initial focal lengths, f_1 and f_2, were selected based on the above analysis and the design flow is summarized in Fig. 10. The Gaussian-beam waist radius in the corrugated horn was 1.2 mm at 275 GHz thus the collimating lens focal was set to $f_1 \approx$ 55 mm to achieve a 20-dB edge taper with the horn and the practical clear-aperture diameter of 60 mm. Equation (2) defined the upper limit of the output Gaussian-beam waist radius. The approximate paraxial limit for Gaussian beams is $w_0 > \lambda/2 \approx 0.68$ mm at 220 GHz. For sufficient marginal, output waist radius of $w_{0,\text{out}} \approx 0.85$ mm was selected yielding a focal length of $f_2 \approx 38$ mm.

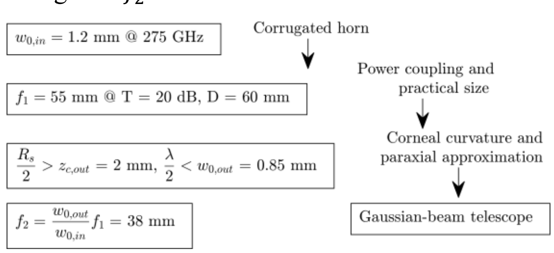

Fig. 10. Logic process to select initial focal lengths f_1 and f_2. The starting points are the available Gaussian-beam waist from corrugated horn antenna and radius of curvature of the cornea, R_s.

B. Lens design via particle-swarm optimization

The aspheric lenses were optimized with a custom ray-tracing algorithm developed in MATLAB. Ray tracing was selected over more accurate PO simulations due to significantly faster computation. Aspheric lens coefficients were found by particle-swarm optimization (PSO). In PSO, a swarm of candidate solutions explores the parameter space and a penalty function is calculated for the particles in the swarm at each iteration [26], [27]. The particles have location and velocity, which are updated in such a way that all the particles tend to stay on their penalty minimum while they converge towards the global penalty minimum. The lens shape was optimized following the procedure in [26], and the particle velocity update equation was:

$$\boldsymbol{v}_{\text{p}}(t+1) = \left[1-\frac{\sqrt{k_{st}\varphi_1}}{2}\right]\boldsymbol{v}_{\text{p}}(t) + k_{\text{st}}\varphi_1(\boldsymbol{p}_{\text{gb}}-\boldsymbol{p}_{\text{p}}) + k_{\text{st}}\varphi_2(\boldsymbol{p}_{\text{ib}}-\boldsymbol{p}_{\text{p}}), \quad (10)$$

where $\boldsymbol{p}_{\text{p}}$ and $\boldsymbol{v}_{\text{p}}$ are current particle position and velocity. $\boldsymbol{p}_{\text{gb}}$ is the global best position of the whole swarm and $\boldsymbol{p}_{\text{ib}}$ is the individual best position of the current particle. $k_{st} = 0.7$ is the stochastic coefficient, φ_1 and φ_2 are random variables with uniform distributions. The position update equation is

$$\boldsymbol{p}_{\text{p}}(t+1) = \boldsymbol{p}_{\text{p}}(t) + \Delta t \boldsymbol{v}_{\text{p}}(t+1), \quad (11)$$

where time step $\Delta t = 1$. In addition, velocity is constrained by $|\boldsymbol{v}_{\text{p}}| \leq \boldsymbol{v}_{\text{max}} = 0.7$ and particle position is limited to the interval $-1 \leq \boldsymbol{p}_{\text{p}} \leq 1$. The particle position in the parameter space was related to the aspheric coefficients in both lens surfaces. For example, for curvature of the first surface:

$$c_{\text{p}}^1 = c_0 + \Delta c p_{\text{p}}^1, \quad (12)$$

where c_0 is the middle value of the first surface curvature, Δc is the maximum deviation from the middle value and p_{p}^1 is the particle position in the 1st dimension of the parameter space. The number of dimensions in the particle space is equal to the number of parameters over which optimization was performed. The lenses were optimized separately, which decoupled the collimating and focusing functions. The lens diameter was fixed at 60 mm and the edge thickness was fixed at 3 mm. These dimensions enable straightforward mounting and assembly of lenses in standard, 76.2-mm optical lens tubes.

The optimization algorithm was run with two different penalty functions: Penalty #1 is the squared transversal aberration at the lens,

$$v(z = z_f) = \frac{1}{N}\sum_{n=1}^{N} {x_n}^2 + {y_n}^2, \quad (13)$$

where x_n and y_n are the coordinates of rays on the focal plane ($z = z_f$) of the lens and N is the number of rays used in the ray tracer. Penalty #2 is the standard deviation of the electric field phase on the curved sample:

$$v(x_c, y_c, y_c,) = \sqrt{\frac{1}{N-1}\sum_{n=1}^{N}(\theta_n - \bar{\theta})^2}, \quad (14)$$

where θ is the electric-field phase on the surface of the curved surface and x_c, y_c, z_c are the corneal surface coordinates. For improved convergence, optimization was initiated with Penalty #1 and switched to Penalty #2 when 25 % of the maximum number of iterations was completed.

C. *Collimating lens*

The collimating lens was optimized enforcing penalty function #1. Fig. 11 shows the ray-tracing result for the first lens. The transversal aberration at the feed-horn position is minimized to 0.010…0.014 λ_0 at the approximate location of the feed waist. To reduce edge illumination and follow the specified overall length of the quasioptics, the feed location was changed from $z = -23$ mm to $z = 0$ mm. As a result, the wave front emanating from the lens is slightly diverging and its effective focal length is 55 mm. The corresponding, comparison hyperbolic lens was designed such that the first surface vertex is coincident with the vertex of the optimized aspheric lens. The second surface of the hyperbolic was planar and positioned to produce the same edge thickness (3 mm) as the aspheric lens.

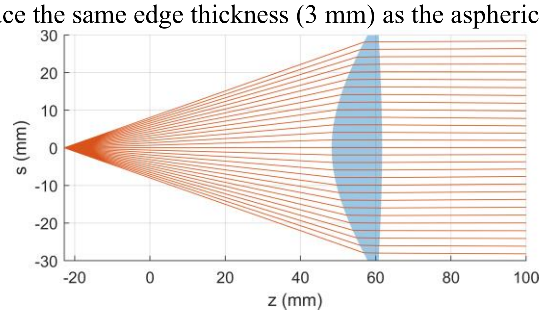

Fig. 11. Ray-tracing result of the optimized aspheric collimating lens. Penalty #1 is used in optimization.

D. *Focusing lens*

The optimization goal for the focusing lens is to minimize the standard deviation of the phase on the curved surface of the sample in pursuit of the plane-wave condition. While the transversal aberration at the focus is minimized by using Penalty #1, with aspheric lenses, it does not guarantee minimal standard deviation of phase on the central part of the cornea. Instead, Penalty #2 considers phase variation and pursues nearly constant phase at the corneal surface up to an *en-face* radius of ~ 1.6 mm (Fig. 13). The ray-tracing results with the second lens optimized with Penalty #1 and Penalty #2 are shown in bottom and top half of Fig. 12, respectively.

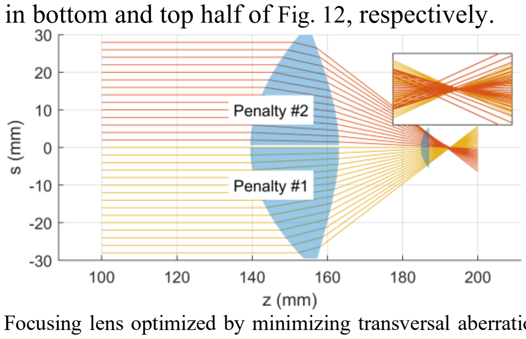

Fig. 12. Focusing lens optimized by minimizing transversal aberration at the center of curvature of the cornea (Penalty #1), and by minimizing the standard deviation of the phase on the curved surface of the cornea (Penalty #2).

Optimization via Penalty #1 produces up to 1.5° phase variation whereas the variation is 0.2° for Penalty #2 in the same range. The effective focal length of the focusing lens is 38.0 mm. The second standard hyperbolic lens is designed with the same criteria as the hyperbolic collimating lens. As the field emanating from the first lens in the practical realization is slightly diverging, the output focus of the second lens appears slightly further away from the lens. However, the results deviate only slightly from the ideal collimated beam. The surface data summary of the custom aspheres and standard hyperbolic lenses are listed in TABLE I.

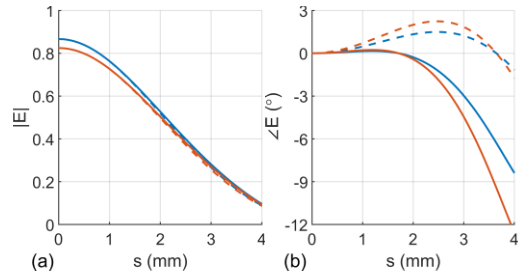

Fig. 13. Electric field a) amplitude and b) phase on the cornea at 220 (blue) and 330 GHz (red) for lenses optimized with Penalty #1 (dashed) and #2 (solid). Phase curves are normalized so that they are zero on axis.

TABLE I

OPTIMIZED COEFFICIENTS FOR ASPHERIC AND HYPERBOLIC LENSES

Aspheric coefficient	Surface 1	Surface 2	Surface 3	Surface 4
Curvature, c	21.2290	-15.8221	15.9580	-23.4501
Conic const., k	-6.1816	-1.5423	-0.9993	-6.7992
Higher order, A_1	2.9636	6.6891	5.4326	0.8307
Higher order, A_2	-8.7153	-0.4383	2.2557	3.9317
Higher order, A_3	5.6511	-7.8445	4.2666	3.3332
Higher order, A_4	0	0	5.7417	8.5735
Higher order, A_5	0	0	3.0480	0.9347
Vertex, t_l	0.0483	0.0617	0.1396	0.163

Hyperbolic coefficient	Surface 1	Surface 2	Surface 3	Surface 4
Focal length, f	0.0483	$-\infty$	∞	0.0371
Vertex, t_l	0.0483	0.0617	0.1396	0.163

V. PHYSICAL-OPTICS SIMULATIONS

Physical-optics simulations of the full quasioptical system were carried out to evaluate aspheric lens performance at 220-330 GHz and to compare it to canonical hyperbolic lens design. The electric field density at the output of the quasioptics on numerous intermediate planes and on the curved surface of the cornea were simulated to determine illumination performance. The reflection back from the curved surface is simulated at the feed horn location for estimating the coupling coefficient of the full quasioptical system. Due to computational time considerations, only the sequential path was considered and effects from multiple paths inside the dielectric lenses were not captured.

A. *Input Gaussian beam from corrugated horn antenna*

The input field to the simulation was a Gaussian-beam waist located at the collimating lens focal point. The waist radius corresponds to a corrugated horn antenna, by Thomas Keating Ltd, operating at WR-3 waveguide band. The antenna was characterized in an antenna measurement range for its directional pattern. Gaussian-beam fits to the directional patterns in E- and H-planes give the waist radii. The designed quasioptics are an approximation of the Gaussian-beam telescope, thus equation (7) is applicable and predicted an output beam waist radius is $w_{0,\text{out}} \approx 0.8$ mm.

B. *Output Gaussian beam on cornea*

The simulated electric field on the curved surface is plotted in Fig. 14 for both lens designs. The left and right columns correspond to the subconfocal and superconfocal positions respectively. The field was simulated at the sub- and superconfocal positions identified in Section II (top two rows of in Fig. 14) as well as an iterated position that minimized the phase variation farther into the corneal periphery (bottom two rows of in Fig. 14). For both aspheric and hyperbolic designs, the field maximum is always on the optical axis at the subconfocal position. At the superconfocal position, the field peak is frequency-dependent and occurs up to ~1 mm off axis. In general, at the superconfocal position, the electric-field distribution is not purely Gaussian, rather it is aberrated due to the near-field effects occurring due to the vicinity of the lens.

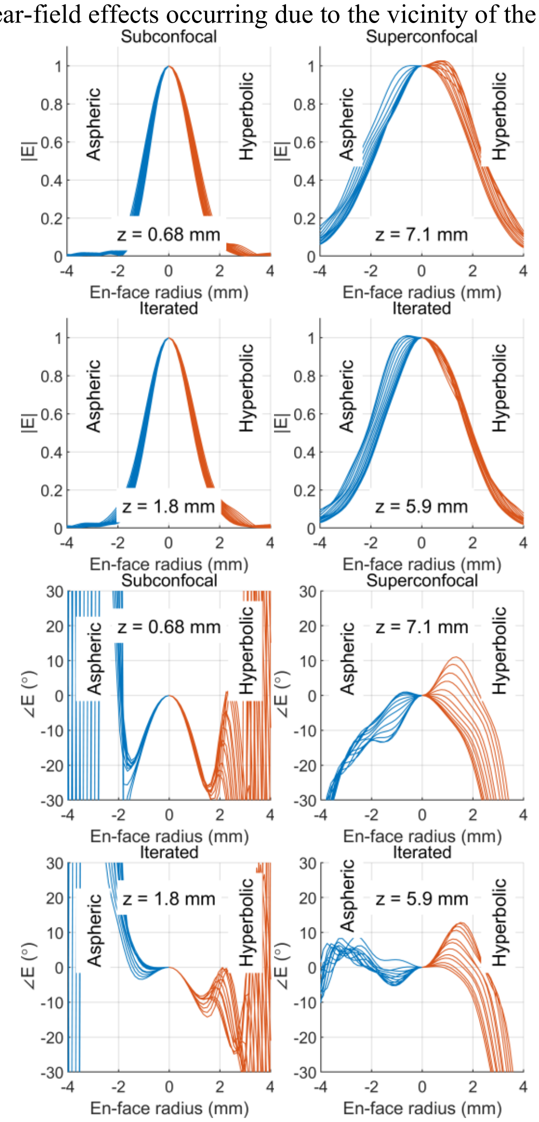

Fig. 14. Simulated electric field the surface of the curved sample at 220-330 GHz. The aspheric design is plotted in blue and the hyperbolic in red. The top rows show when the cornea is at the subconfocal and superconfocal positions from Equation (1). The bottom rows show the positions from the PO simulation.

At the subconfocal position (Equation (1)), the phase on cornea varies up to 10° for the aspheric and hyperbolic designs within the half-maximum beam radius. Conversely, at the superconfocal position, the phase varies 13° and 25° for the aspheric and hyperbolic designs, respectively. The iterated, subconfocal position, identified by the PO simulations results in 3° and 10° phase variations for aspheric and hyperbolic designs, respectively, within the half-maximum beam radius. Across the whole curved surface, the iterated superconfocal position ($z = 5.9$ mm) results in 20° peak-to-peak phase variation. This result is consistent with the ray-tracing results optimized with Penalty #2 (Fig. 13).

Two key findings arise from this analysis. (1) The design criteria calling for the mapping of a collimated beam to a spherical phase front seems to specify a canonical diffraction limited optics, namely a plano-hyperbolic lens that produces a diffraction limited spot in the focal plane. However, with respect to these design parameters, optimizing a cost function defined on a sphere whose center of curvature is concentric with the location of circle of least confusion is not equal to optimizing canonical lens at the focal plane. In this case, the customized, biconvex aspheric optics always outperforms the plano-hyperbolic lens. (2) The lens design and optimization were performed with respect to superconfocal operating condition as this region is further from the Gaussian beam waist and is inherently more broadband. However, due to the short lens focal lengths necessary for phase front matching to the 7.5 mm RoC cornea, the beam field falls into the lens aperture near field. Near field aberrates the Gaussian beam phase front. These effects, combined with the smaller overall, on-cornea beam radii result in the subconfocal position always outperforming the superconfocal position. These two findings are counterintuitive from a geometric optics standpoint and arise from the very small cornea and aperture dimensions with respect to the illumination wavelength.

VI. Experimental Work

Lenses for the aspheric design were manufactured from TOPAS via CNC lathe (Oplatek Oy, Finland). The two lenses were assembled inside a 76.2-mm lens tube and positioned with threaded retaining rings. To reduce internal reflections, the inside of the lens tube was lined with millimeter-wave absorber (ECCOSORB LS-22 by Emerson & Cuming). The quasioptical system was fed with a millimeter-wave extender (WR3.4-VNAX by Virginia Diodes Inc.) driven by a vector network analyzer (N5225B PNA by Keysight Technologies). The quasioptical performance was first evaluated with a near-field measurement range (NSI 200V-5×5 by Near-Field Systems Inc.) shown in Fig. 15 a. The *ex vivo* and *in vitro* test setup is displayed in Fig. 15 b and shows the quasioptics oriented vertically allowing the cornea phantoms and *ex vivo* corneas to point upwards during measurements. The vertical configuration ensured that gravity would affect sample fluids, geometry, and water content symmetrically about the optical axis.

A. *Field at the lens apertures*

The specified manufacture tolerance of the lenses was $\lambda_{330\ \mathrm{GHz}}/20 \approx 45$ µm. Five copies of the collimating lens were manufactured and characterized in the antenna near-field test range (Fig. 15 a). A WR-3 open-ended waveguide was used as an E-field probe. The measurement was scanned a 20 mm x 20 mm plane at 40 mm from the vertex of the collimating lens where the converging beam has an edge taper of at least -35 dB. The feed position was adjusted to produce a planar output wavefront. The median of all measured wave fronts was subtracted from measured field data to obtain differential measurements and thus estimates of manufacturing accuracy. The maximum differential of the five lenses is up to 32 % in amplitude and up to 23° in phase. The phase difference is within the specification up to ~ 320 GHz and exceeds it slightly at 330 GHz. The near field immediately following the focusing lens was measured and the field on the lens is calculated with the PO algorithm described in Section IV. Fig. 16 shows the normalized amplitude at the surface of the second lens, where the edge taper is 30 dB.

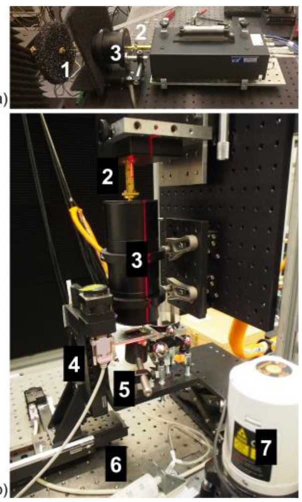

Fig. 15. a) Partly assembled system for evaluating the quality of manufacture of the collimating lens. b) Fully assembled system while ongoing *ex vivo* sheep cornea measurement. 1) open-ended waveguide in near-field measurement, 2) corrugated horn antenna, 3) lens tube, 4) x, y, and z translational stages, 5) cornea sample and calibration targets, 6) arrangement for hydrostatic pressure adjustment, and 7) line laser indicating the optical axis of the quasioptics.

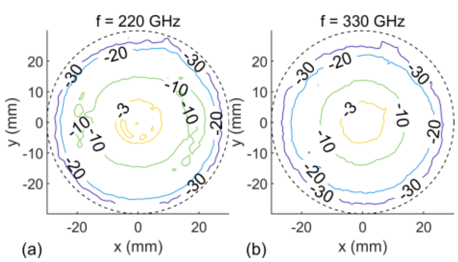

Fig. 16. Normalized electric field calculated at the surface of the second lens at a) 220 and b) 330 GHz. The lens aperture is shown with dashed line.

B. Field around the output beam waist

The electric field calculated with the PO algorithm at the focus of the quasioptical system is compared to the simulation. Fig. 17 shows the E- and H-plane electric field at the output beam waist demonstrating a good agreement between the simulation and experiment. At 330 GHz, the differences increase below −20 dB; up to 10 dB. The off-axis ripple is typically larger in the measurements than in the simulations and may be due to the non-Gaussian nature observed in the aperture field. Gaussian beams were fitted to the simulated and measured data to estimate the output beam waist radius as displayed in Fig. 18.

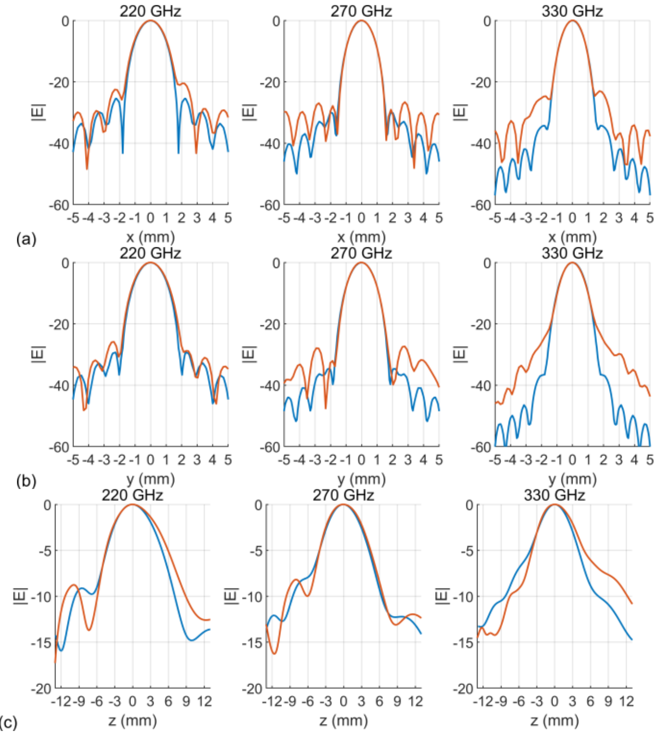

Fig. 17. Simulated (blue) and measured (red) electric field at the location of the output focus of the quasioptics for a) H-planes, b) E-planes, and c) on the optical axis. The fields are normalized to their maximum.

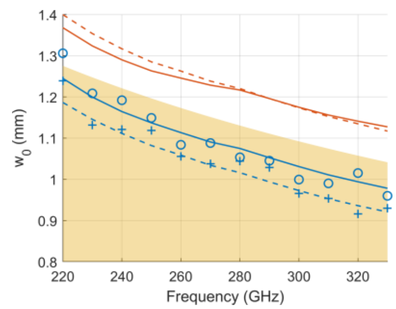

Fig. 18. Gaussian-beam radius for the aspheric (blue) and hyperbolic (red) designs. Simulated and measured radius for the aspheric design is within match criterion (shaded). Both E- (solid, "o") and H-plane (dashed, "+") shown.

The oscillatory variation in measured waist shows a period of ~40 GHz. This variation may be due to internal reflections in the quasioptics, which are difficult to model and were not included in the PO simulation. The waist radius for the aspheric design is always less than the maximum waist computed for the ideal Gaussian beam. Conversely, the waist radius produced by the hyperbolic design is always larger suggesting that the hyperbolic design would not result in an optimum match between a Gaussian beam and a curved surface.

C. Field on spherical surface

The measured planar near-field data and PO algorithm was used to estimate the field on a virtual surface corresponding to a sphere with $R_s = 7.5$ mm. The transverse location is iterated until the vertex of the surface is accurately centered in the electric field. The iterated positions were evaluated at all frequencies and the best fit identified as an average across the band. This transverse position was labeled the optical axis. The normalized electric field on the curved surface is shown in Fig. 19.

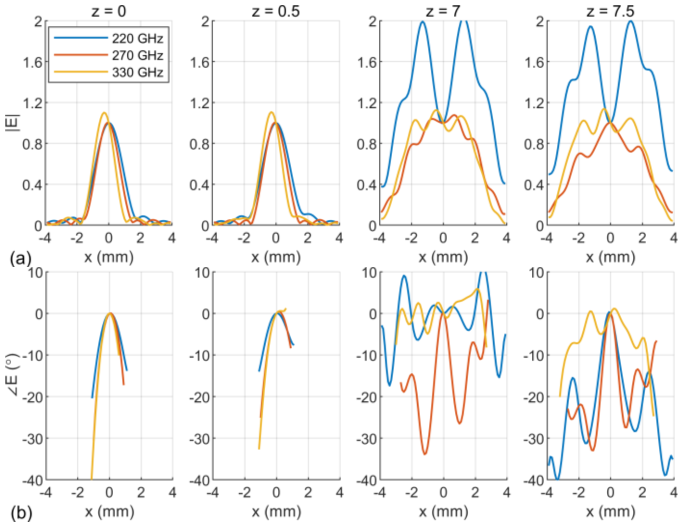

Fig. 19. The measured electric field a) amplitude and b) phase calculated on a curved surface ($R_S = 7.5$ mm) with its vertex at 0 to 7.5 mm from the beam waist. Phase is displayed down to normalized field amplitude of $\exp(-1)$.

Close to the waist and subconfocal position from the Gaussian-beam theory ($z = 0$ mm and $z = 0.5$ mm), the field decays below $1/e$ within a 1-mm distance from the axis. The phase decreases monotonically further out from the axis with relatively frequency-independent behavior. Conversely, the field varies more at the superconfocal position from Gaussian-beam theory ($z = 7.0$ mm). The amplitude distribution does not always peak at the optical axis and the phase varies significantly. Within the given frequency range and dimensions of the quasioptics, the Gaussian nature of the output beam did not hold far from the waist location, rather, the near-field effects significantly affected the beam quality at the superconfocal position. Consequently, the observed reflection coefficient will deviate from the theory and limit CCT and CTWC measurement sensitivity.

D. Coupling to spherical reflector

Quasioptical coupling to reference reflectors was measured by scanning the position of the spherical and planar mirrors in the output beam of the quasioptical system, as shown in Fig. 20. The planar mirror scan enabled assessment of beam waist position as the peak return occurred when the mirror was coplanar with the waist. The spherical reflector reflection was referenced to the beam-waist location by measuring the delay between peaks in the time-domain transformation of the measured, frequency-domain S_{11} parameters. Fig. 21 shows the frequency integrated S_{11} measured for the planar and spherical mirrors. The peak amplitude S_{11} is 0.65 and 0.63 for the planar and spherical reflectors, respectively. Compared to the simulated coupling efficiency (Fig. 5), the experimental results show poor coupling at a superconfocal position of ~ 7 mm. This likely due to the nearfield effects discussed above. At ~ 1 mm (subconfocal), coupling from the spherical reference reflector was maximized. Measurements of corneal phantoms as well as *ex vivo* corneas were performed in the vicinity of this position.

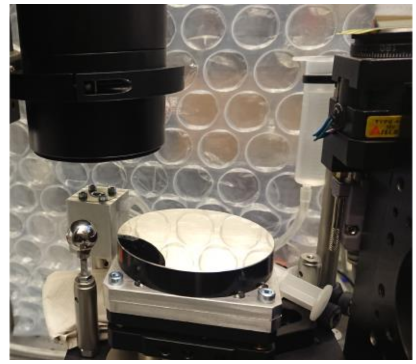

Fig. 20. Quasioptical system being aligned with the spherical ($R_s = 7.50$ mm) and planar reflector.

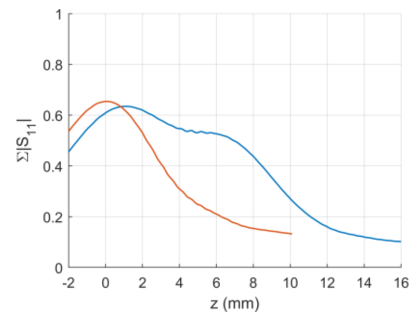

Fig. 21. Measured coupling to the spherical (blue) and planar (red) reflectors integrated across the 220-330 GHz band. Maximum coupling to planar mirror indicates the beam waist location. The maximum coupling to spherical reflector occurs at about 1 mm from the beam waist.

VII. MEASUREMENTS WITH PHANTOMS AND CORNEA

The quasioptical system was used to extract the thickness and water content from the cornea phantoms and *ex vivo* sheep corneas. The corneal phantom was a contact lens; brand name Acuvue Moist. It was made of silicon hydrogel called Comfilcon A and its central thickness was ~ 250 μm as measured with an optical microscope. The phantom was installed in a phantom holder to replicate the conditions of the actual cornea and anterior chamber: The phantom was backed with physiological saline solution (0.9 % NaCl water solution) at a simulated intra-ocular pressure of 980 Pa. The data was analyzed with a saline water permittivity model for millimeter waves [28], that the authors reported should be usable up to 500 GHz. Fig. 22 shows the corneal phantom holder with installed contact lens and a microscopic photo of its cross section. The thickness of the contact-lens phantom reduces towards the periphery and it is about 170 μm at radius of 2 mm. The contact lens water content listed by the manufacturer varies between 48 % and 52 %. Individual lenses were measured with an accurate scale and water content corroborated through ratios of dry weight to wet weight. Contact lens wet mass was measured immediately following removal from its package. Dry mass was acquired following overnight placement in a silica-gel desiccator. These measurements indicate a hydrated water content ranging from 55 % to 60 %.

Ex vivo sheep eyes were placed in a mount that exerts an even force distributed via a 12-mm retaining ring around the corneal periphery. The ring stabilizes the corneal surface position and ensures a spherical profile. A column of saline solution for pressure maintenance was coupled, via a rigid catheter, to the anterior chamber of the eye. The healthy cornea has a total water content of ~ 78 % [29], [30]. The sheep eyes were acquired from a local butcher shop and the elapsed time between harvesting and measurement with the quasioptical system was ~12 to 36 hours. The eyes were stored and transported in saline solution at 2 – 3 °C until measured. Attempts were made to measure *ex vivo* corneal thickness with an ultrasound pachymeter (PachPen, Accutome Inc.). However, significantly difficulties were faced when coupling the pachymeter measurement head to the corneal tissue. Fig. 23 reports CCT measurements with ultrasound pachymeter with the eye installed in the sample holder. The measurements ranged from 490 μm to 900 μm.

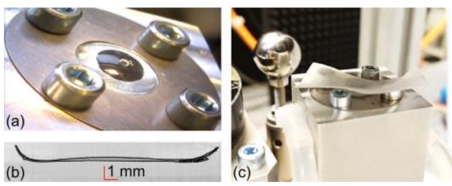

Fig. 22. a) Corneal phantom holder. The void under the phantom simulates the anterior chamber of the eye. b) Microscopic image of halved and flattened phantom. The black contour emphasizes the edges. The central thickness of the phantom is 250 μm. c) Corneal phantom being wetted with a paper towel.

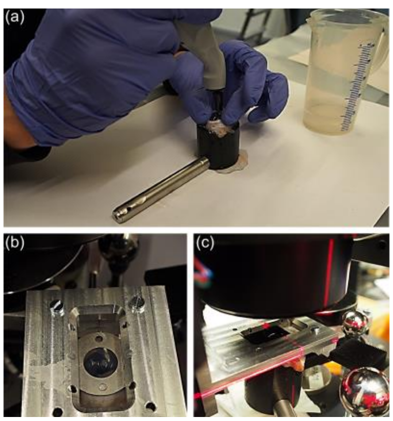

Fig. 23. a) *Ex vivo* sheep cornea being measured for its thickness with an ultrasound pachymeter, b) cornea sample with injection needle inserted to the anterior chamber (upper right quadrant of the cornea) to provide physiologically relevant intra-ocular pressure, and c) cornea sample aligned with the quasioptical system with a line laser showing the optical axis and beam waist position. The cornea is surrounded with TK THz RAM absorbing material in order to prevent reflections from the retaining ring.

A. Parameter extraction

Reflectivity measurements (S_{11}) of the reference spherical reflector were acquired immediately prior to and following the phantom and *ex vivo* cornea measurements to calibrate reflectivity data and remove confounders due to system drift. To ensure optimal sample position with respect to the measurement system's aperture, the mounted phantom and corneas were raster and height scanned beneath the quasioptics.

Particle-swarm optimization was used to obtain sample thickness and water content. Following the principles presented in Sections II and III. C, the sample was carefully aligned to the subconfocal position. This let us assume the normal incidence angle on the sample and stratified medium model with corneal (phantom) tissue thickness and water content as parameters was employed. Further, the model included a thin layer of water lying atop the sample to account for surface water arising from surface tension as well as water transport through the sample due to pressure in the sample holder and anterior chamber. Time gating is used to separate the sample reflection from the reflections within the quasioptics. The distance between aperture and sample could not be controlled to fractions of a wavelength. Additionally, while the samples were prepared and mounted to minimize radius of curvature differences between the anterior surface and the spherical reference reflector, a specific sample radius of curvature and distance could not be guaranteed. The resulting uncontrolled distance added a phase delay, which likely varied from sample to sample and between sample and reference reflector. Thus, a fit to the linear part of the S_{11} phase was subtracted from the gated measurements and particle-swarm fitting considered only the non-linear part of the phase.

The experimental reflection coefficient and PSO-derived fits are shown in Fig. 24. The dry relative permittivity of the silicone hydrogel was fixed at 2. The fit (Fig. 24 a) demonstrates sufficient agreement to the calibrated reflection coefficient and corresponds to a thickness of 256 μm, a tear-film thickness of 10 μm, and water content of 45 %. The contact lens is exposed to atmosphere for ~ 30 minutes during alignment process, prior to the actual measurement. This may result in significant drying at the front surface of the lens resulting in a lower-than-expected water content and/or uneven distribution of water. Water may also occur in either a bound or unbound state in the material, which results in deviation from the saline-water model. Bound, water is reported to have smaller permittivity [1], [3], [7], than free water and this difference is in line with the observed lack of water. Consideration of bound water permittivity and uneven contact lens layer thickness may improve the fit.

Example of the observed reflection coefficient for *ex vivo* sheep cornea is shown in Fig. 24 b. The cornea RoC depends on manual preparation of the sample and efforts were made to match to the curved reflector. Again, the fit to the observed reflection coefficient follows the experiment. This time, possibly due to improved curvature match, the observed reflection coefficient phase is more similar to the model than with the phantom. All the fits were done with data ranging from 250 to 320 GHz, as high phase ripple persists below 250 GHz and the edges of the bandwidth suffer from gating artefact. This is likely due to sub-optimal performance of the corrugated horn below 250 GHz.

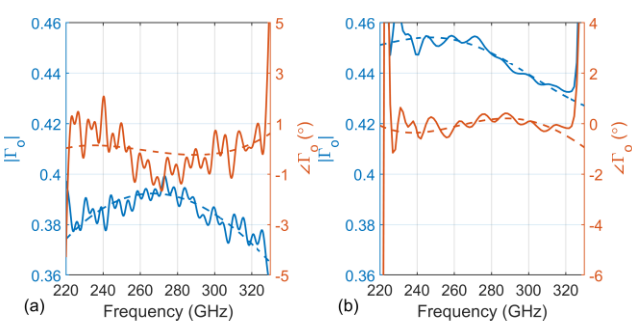

Fig. 24. Reflection coefficient for a) contact lens and b) sheep cornea. The stratified medium model (dashed) is fit the measured reflectivity (solid) with the PSO algorithm.

In total, 20 *ex vivo* sheep corneas were measured and CCT, CTWC and TFT extracted. The corneas were measured in three batches throughout a three-month campaign with the setup partially re-assembled and mechanically improved in successive batches. The extracted parameters are shown in Fig. 25 and associated fit statistics shown in TABLE III. The cornea model was a homogenous layer of collagen with dry permittivity of 2.9. Two of the fits produced unrealistically small CCT and were considered erroneous. The rest of the cornea show thicknesses ranging from ~ 500 µm to ~ 800 µm. In comparison, *in vivo* sheep cornea is ~ 650-µm thick [31]. The tear-film thickness shows variation from 0 µm to 50 µm, which is realistic considering the experimental conditions: a small water layer may lay on the cornea as well as evaporate during the measurement. The corneal-tissue water content is remarkably invariant from sample to sample, especially for sample numbers 16 - 20, with an average of 47 %. While the total water content of healthy cornea is ~ 78 % by mass [29], [30] a significant fraction is bound resulting in a lower submillimeter wave permittivity than what is expected when the entire water volume is free. Numerous references report bound water relative permittivity between 2.5 to 3 in [7], [16], [17], and relatively low value in [32]. Bounding of water would hence show up as an absence of water, as there is only small permittivity contrast to collagen.

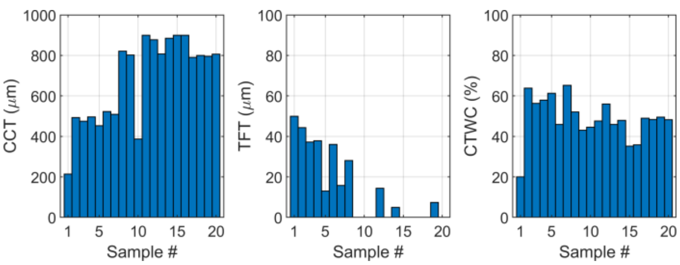

Fig. 25. Fitted CCT, TFT, and CTWC for 20 *ex vivo* sheep corneas. The corneas have been measured in three batches: 1-6 (December 2018), 7-12 (January 2019), and 13-20 (February 2019).

To study the effect of water evaporation from the phantom surface, the phantom was covered with a paper towel saturated with saline solution. The duration of coverage was about ~60 s, after which the towel was removed. At the same time, a time-series measurement of reflection was run with complex S_{11} acquired every ~ 6 s. The parameters fitted to the time series show 10-µm tear-film thickness just after the towel is removed (Fig. 26).

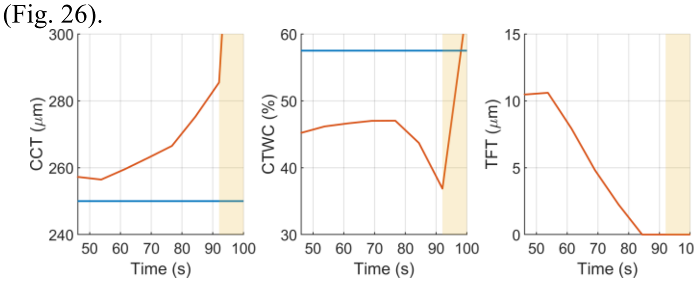

Fig. 26. Parameter fit to water dynamics in the corneal phantom. At 46 s, the towel saturated with saline solution is taken off the phantom surface. Nominal thickness and water content (blue) are predicted sufficiently at first. Predicted thickness increases as well as water content up to 76 s. At the same time, tear-film thickness decreases close to linearly. Water content drops once the tear-film has depleted. The parameter fit is unsuccessful in the shaded area.

After that the tear-film thins and phantom seems to get thicker as well as the water content increases slightly. At ~ 76 s, the water content starts to reduce fast to less than 30 %, indicating drying after the tear film has been depleted.

TABLE II

EXTRACTED PARAMETERS FOR SHEEP CORNEA

Parameter	Mean	Standard deviation
CCT (µm)	652	196
TFT (µm)	14	7
CTWC (%)	47	8

VIII. DISCUSSION AND CONCLUSIONS

Submillimeter-wave sensing is well suited to measure corneal water content, corneal thickness, and tear-film thickness in cornea. This work considered the design space for efficient, optimal submillimeter-wave coupling to the cornea. We have identified optimal alignment of a Gaussian beam on cornea and considered quasioptical arrangements to achieve optimal alignment. The dimensions of the cornea, the wavelength, and the practical design aspects together set boundary conditions to the alignment and quasioptical design. Extracting corneal parameters from observed complex reflection coefficients is based on inversing a model constructed with the stratified medium theory which assumes plane waves incident on planar media. To be faithful to theory, locally plane-wave like illumination with normal incidence is required. In other words, optimal coupling to corneal tissue occurs at specific offsets between beam waist and corneal apex/CoC that depend on the illumination Gaussian beam properties. In general, alignment with the sample is not arbitrary but rather a strict requirement set by the small radius of curvature of the cornea as well as the desired limited illuminated area. For the curved corneal surface, Gaussian beam illumination with a frequency-independent confocal distance results in efficient, broadband coupling. We have identified the optimal coupling to occur at the subconfocal and superconfocal distances from the Gaussian beam waist for beams with sufficiently small confocal distance z_c. From a geometric optics perspective, the superconfocal distance appears most suitable for coupling to an ideal curved surface. However, small differences between the calibration target and cornea will result in large error in the observed reflection coefficient. The subconfocal distance on the other hand results in corneal sensing that is insensitive to errors arising from the geometrical inaccuracies in the sample and calibration reflector.

Designs based on aspheric and hyperbolic dielectric lenses were considered, which result in differing field distributions on the corneal surface. Phase-coherent ray tracing and physical optics simulations identified specific aspheric lens sag coefficients suitable for corneal sensing applications. The practical realizations of short focal length quasioptics may give rise to near-field effects that the fundamental-mode Gaussian-beam theory cannot replicate. These near-field effects were confirmed by simulation and measurements suggest that the subconfocal distance is the optimum for corneal sensing as it lies further from the radiating aperture. Further, the beam at the subconfocal distance is limited to the central part of the cornea, where the effect of the radial thickness gradient is the least.

The optimized lens design aims to create plane-wave like conditions on the corneal surface and the standard deviation of the electric field phase on the corneal surface was minimized. In the future, the use of aspheric surfaces may allow for more elaborate illumination engineering, e.g., a constant amplitude distribution on the cornea. It may also be possible to tailor aspheric surfaces to the source profile and create an output beam with truly frequency-independent confocal distance. However, while the combination of corrugated antenna and custom aspheric lenses resulted in a near-constant confocal distance at 220-330 GHz, synthesis methods that model the near-field effects should be considered to improve upon this performance.

A measurement campaign with corneal phantoms and *ex vivo* sheep corneas was completed. The contact lens was used as a phantom model due to its water permeability and dielectric permittivity that is similar to collagen; the majority non-aqueous constituent of cornea. The contact lens was mounted on a sealed phantom holder and backed by a physiologically relevant saline solution. The solution was kept in static pressure similar to known human eye intra-ocular pressure. Contact lenses, however, are thin compared to the cornea and with a decreasing thickness for increasing radius differ in the thickness profile from the cornea. For more realistic experiments, the corneal phantom with physiologically meaningful geometry and permittivity should be used. As a step towards the realistic use case, reflectivity of *ex vivo* sheep corneas was measured. The aqueous humor pressure was maintained at physiologically relevant levels during the measurements. The phantom water content and thickness are predicted with close to manufacturers quoted values and our own alternatively determined values. The phantom central thickness is predicted accurately close to our microscopic study. Parameters are predicted for 20 *ex vivo* sheep corneas and they show very similar sample-to-sample water content, 47 % on average. We deduce that the low permittivity, about 3 according to literature, of bounded water in the cornea reduces the apparent water content from the expected 78 %. In our case, this suggests that about 60 % of the total water in the cornea is free water. The median value of the predicted sheep cornea thickness is close to the literature values, although variation of the predicted thickness is quite large – partly due to actual physiological variations and partly due to the remaining inaccuracies in matching to the cornea surface. These first results show clearly that accurate submillimeter-wave measurements of corneal reflectivity can be carried out with such a quasioptical setup and that stratified medium theory can be used to predict the physiologically meaningful parameters from corneal phantoms and cornea. In addition, we are able to track the water-transport phenomena in and on corneal phantom, as the measured tear-film thickness and water content indicate drying.

ACKNOWLEDGEMENTS

Ms. Mariangela Baggio and Dr. Irina Nefedova are thanked for the help with the *ex vivo* cornea measurements. The simulations presented above were performed using computer resources within the Aalto University School of Science "Science-IT" project. All the submillimeter-wave experiments are conducted in MilliLab, an external research laboratory to European Space Agency. Corneal phantom water content measurements are done at Aalto University School of Chemical Engineering.

REFERENCES

[1] S. Qiushuo, E. P. J. Parrott, Y. He, and E. Pickwell-MacPherson, "In vivo THz imaging of human skin: Accounting for occlusion effects," *Journal of Biophotonics*, vol. 11, no. 2, e201700111, 2018.

[2] Z. D. Taylor, J. Garritano, S. Sung, N. Bajwa, D. B. Bennett, B. Nowroozi, P. Tewari, J. Sayre, J.-P. Hubschman, S. Deng, E. R. Brown, and W. S. Grundfest, "THz and mm-wave sensing of corneal tissue water content: electromagnetic modeling and analysis," *IEEE Transactions on Terahertz Science and Technology*, vol. 5, no. 2, pp. 170-183, 2015.

[3] I. Ozheredov, M. Prokopchuk, M. Mischenko, T. Safonova, P. Solyankin, A. Larichev, A. Angeluts, A. Balakin, and A. Shkurinov, "In vivo THz sensing of the cornea of the eye," *Laser Physics Letters*, vol. 15, no. 5, p. 055601, 2018.

[4] A. A. Angeluts, A. V. Balakin, M. D. Mishchenko, I. A. Ozheredov, M. N. Prokopchuk, T. N. Saphonova, A. P. Shkurinov, "Application of THz reflectometry to eye cornea hydration measurements," *Proceedings of 41st International Conference on Infrared, Millimeter, and Terahertz waves (IRMMW-THz)*, Demark, 2016, pp. 1-2.

[5] S. Sung, S. Dabironezare. N. Llombart, S. Selvin, N. Bajwa, S. Chantra, B. Nowroozi, J. Garritano, J. Goell, A. Li, S. X. Deng, E. Brown, W. S. Grundfest, and Z. D. Taylor, "THz Imaging System for in vivo Human Cornea," *IEEE Transactions on Terahertz Science and Technology*, vol. 8, no. 1, pp. 27-37, 2018.

[6] Z. D. Taylor, J. Garritano, S. Sung, N. Bajwa, D. B. Bennett, B. Nowroozi, P. Tewari, J. W. Sayre, J.-P. Hubschman, S. X. Deng, E. R. Brown, and W. S. Grundfest, "THz and mm-wave sensing of corneal tissue water content: In vivo sensing and imaging results," *IEEE Transactions on Terahertz Science and Technology*, vol. 5, no. 2, pp. 184-196, 2015.

[7] A. Sihvola, *Electromagnetic Mixing Formulas and Applications*, IEE, Electromagnetic Waves Series 47, 1999.

[8] S. Sung, S. Dabironezare, N. Llombart, S. Selvin, N. Bajwa, S. Chantra, B. Nowroozi, J. Garritano, J. Goell, A. Li, S. X. Deng, E. Brown, W. S. Grundfest, and Z. D. Taylor, "Optical system design for noncontact, normal incidence, THz imaging of in vivo human cornea," *IEEE Transactions on Terahertz Science and Technology*, vol. 8, no. 1, pp. 1-12, 2018.

[9] D. B. Bennett, W. Li, Z. D. Taylor, W. S. Grundfest, and E. R. Brown, "Stratified media model for terahertz reflectometry of the skin," *IEEE Sensors Journal*, vol. 11, no. 5, 2011, pp. 1253-1262.

[10] N. Morita, T. Tanaka, T. Yamasaki, and Y. Nakanishi, "Scattering of a beam wave by a spherical object," *IEEE Transactions on Antennas and Propagation*, vol. 16, no. 6, pp. 724-727, 1968.

[11] E. E. M. Khaled, S. C. Hill, and P. W. Barber, "Scattered and internal intensity of a sphere illuminated with a Gaussian beam," *IEEE Transactions on Antennas and Propagation*, vol. 41, no. 3, pp. 295-303, 1993.

[12] L. Y. Hei and R. Leonhardt, "Aspheric lenses for terahertz imaging," *Optics Express*, vol. 16, no. 20, pp. 15991-15998, 2008.

[13] I. Ozheredov, M. Prokopchuk, M. Mischenko, T. Safonova, P. Solyankin, A. Larichev, A. Angeluts, A. Balakin, A. Shkurinov, "In vivo THz sensing of the cornea of the eye," *Laser Physics Letters*, vol. 15, no. 5, 055601.

[14] E. L. Martola and J. L. Baum, "Central and peripheral corneal thickness: a clinical study" *Archives of Ophthalmology*, vol. 79, no. 1, pp. 28-30, 1968.

[15] S. J. Orfanidis, *Electromagnetic Waves and Antennas*, 2003.
[16] S. I. Alekseev and M. C. Ziskin, "Human skin permittivity determined by millimeter wave reflection measurements," *Bioelectromagnetics*, vol. 28, no. 5 pp. 331-339, 2007.
[17] S. I. Alekseev, I. Szabo, and M. C. Ziskin, "Millimeter wave reflectivity used for measurement of skin hydration with different moisturizers," *Skin Research and Technology*, vol. 14, no. 4, pp. 390-396, 2008.
[18] Goldsmith, Paul F. *Quasioptical systems*. Chapman & Hall, 1998.
[19] J. Yao, J. Ma, J. Zhao, P. Qi, M. Li, L. Lin, L. Sun, X. Wang, W. Liu, and Y. Wang, "Corneal hydration assessment indicator based on terahertz time domain spectroscopy," *Biomedical Optics Express*, vol. 11, no. 4, pp. 2073–2084, 2020.
[20] A. Chen, O. Osman, Z. Harris, A. Abazri, R. Honkanen, and M. Arbab, "Investigation of water diffusion dynamics in corneal phantoms using terahertz time-domain spectroscopy," *Biomedical Optics Express*, vol. 11, pp. 1284-1297, 2020.
[21] J. Sherman, "Properties of focused apertures in the fresnel region," *Transactions on Antennas and Propagation*, vol. 10, no. 4, pp. 399-408, 1962.
[22] Kong, J. A. *Electromagnetic Wave Theory*, John Wiley & Sons, New York, 1986.
[23] B. H. Walker, *Optical Design for Visual Systems*, vol. 45. Bellingham, WA, SPIE Press, 2000.
[24] W. J. Smith, *Modern Optical Engineering*, SPIE Press, McGraw-Hill, 2000.
[25] E. Gandini, A. Tamminen, A. Luukanen, and N. Llombart, "Wide field of view inversely magnified dual-lens for near-field submillimeter wavelength imagers," *IEEE Transactions on Antennas and Propagation*, vol. 66, no. 2, pp. 541-549, 2018.
[26] M. Clerc and J. Kennedy, "The particle swarm - explosion, stability, and convergence in a multidimensional complex space," *IEEE Transactions on Evolutionary Computation*, vol. 6, no. 1, pp. 58-73, Feb. 2002.
[27] J. Robinson and Y. Rahmat-Samii, "Particle swarm optimization in electromagnetics," *IEEE Transactions on Antennas and Propagation*, vol. 52, no. 2, pp. 397-407, Feb. 2004.
[28] T. Meissner and F. J. Wentz, "The complex dielectric constant of pure and sea water from microwave satellite observations," *IEEE Transactions on Geoscience and Remote Sensing*, vol. 42, no. 9, pp. 1836-1849, 2004.
[29] C. A. Greene, S. L. Misra, H. Lee, J. McKelvie, K. Kapadia, R. McFarlane, C. N. J. McGhee, C. R. Green, and T. Sherwin, "The sheep cornea: structural and clinical characteristics," *Current Eye Research*, vol. 43, no. 12, pp. 1432-1438, 2018.
[30] M. Biswaranjan, S. K. Mishra, and D. K. Majumdar, "Effect of formulation factors on in vitro transcorneal permeation of voriconazole from aqueous drops," *Journal of Advanced Pharmaceutical Technology and Research*, vol. 4, no. 4, pp. 210-216, 2013.
[31] A. J., LoPinto, C. G. Pirie, D. Bedenice, and S. L. Ayres, "Corneal thickness of eyes of healthy goats, sheep, and alpacas manually measured by use of a portable spectral-domain optical coherence tomography device," *American Journal of Veterinary Research*, vol. 78, no. 1, pp. 80-84, 2017.
[32] H.P. Schwan, "Electrical properties of bound water," *Annals of the New York Academy of Sciences*, vol. 125, no. 2, pp. 344-354, 1965.

Aleksi Tamminen was born in Ruotsinpyhtää, Finland, in 1982. He received the B.Sc. (Tech.) and M.Sc. (Tech.) degrees from the Helsinki University of Technology, Espoo, Finland, in 2005 and 2007, respectively. He received the Lic.Sc. (Tech.) and D.Sc. (Tech.) degrees from Aalto University (former Helsinki University of Technology), Espoo, in 2011 and 2013, respectively. From 2005 to 2013, he was with the Department of Radio Science and Engineering, Aalto University. His research work in Aalto University was related to antenna measurements and imaging at millimeter and submillimeter waves. In addition to research, he served as the organizing secretary of international conference, 6th ESA Workshop on Millimetre-Wave Technology and Applications and 4th Global Symposium on Millimeter Waves, held in Espoo in May 2011. He has authored or co-authored about 40 scientific journal and conference publications as well as three patent applications. He received the Young Engineer Prize from the 5th European Radar Conference on 31st November 2008 as well as the Best Student Paper Award from the Global Symposium on Millimeter Waves 2010 on 14th –16th April 2010. From 2013 to 2018 he was Research Scientist at Asqella Ltd., Helsinki, Finland. He was the principal in the research and development of commercial submillimeter-wave imaging technology as well as in participating in academic research projects in the related field. From 2018, he is with Aalto University as Research Fellow. His current research interests are submillimeter- and millimeter-wave projects including antenna measurements, sensing biological tissues, and imaging.

Samu-Ville Pälli was born in Savonlinna, Finland, in 1994. He received the B.Sc. (Tech.)(Hons.) and M.Sc. (Tech.)(Hons.) degrees in electrical engineering from Aalto University, Espoo, Finland, in 2018 and 2020, respectively. He has been with the Department of Electronics and Nanoengineering, Aalto University School of Electrical Engineering, since 2017, where he is currently pursuing the D.Sc. (Tech.) degree. His current research interest includes submillimeter- and millimeter-wave imaging.

Juha Ala-Laurinaho received the Diploma Engineer (M.Sc.) degree in mathematics and D.Sc. (Tech.) degree in electrical engineering from TKK Helsinki University of Technology, Finland, in 1995 and 2001, respectively. He has been with the TKK, currently Aalto University, serving in the Radio Laboratory in 1995–2007, in the Department of Radio Science and Engineering in 2008-2016, and currently in the Department of Electronics and Nanoengineering. Currently, he works as a Staff Scientist. Dr. Ala-Laurinaho has been a Researcher and Project Manager in many millimeter wave technology related projects. His current research interests are the antennas and antenna measurement techniques for millimeter and submillimeter waves, and the millimeter wave imaging.

Mika Salkola received the Diploma Engineer M.Sc. (Tech.) degree in control engineering and software engineering from Helsinki University of Technology, Finland (TKK) in 1991. He has extensive and versatile experience in R&D both in engineering and managerial positions. He has over 20 years of experience in international R&D operations in high technology companies, among others at Thermo Fisher Scientific and Vaisala. He is the inventor or co-inventor of several patent applications, one of them describes utilization of millimeter and submillimeter wavelengths for sensing biological tissue. In addition he has instructed ten bachelor or master of science thesis works. At the moment he is working for Revenio Group Oyj as Development Director of Icare Finland Oy and Research and Development Director of Revenio Research Oy.

Antti V. Räisänen (F'94 – LF'16) received the D.Sc.(Tech.) degree in EE from the Helsinki University of Technology (TKK) (now Aalto University), Espoo, Finland, in 1981. In 1989, he was appointed Professor Chair of Radio Engineering with TKK, after holding the same position pro tem in 1985 and 1987–1989. He has been a Visiting Scientist or Professor with Five College Radio Astronomy Observatory (FCRAO) and the University of Massachusetts at Amherst (1978–1979, 1980, 1981); the Chalmers University of Technology (1983); the University of California at Berkeley (1984–1985); the Jet Propulsion Laboratory (JPL) and California Institute of Technology (1992–1993); Observatoire de Paris and Universite de Paris 6 (2001–2002), and Universidad Carlos III de Madrid (2013-2014).

He has supervised a large number of master and doctoral students in millimeter-wave components, antennas, receivers, microwave measurements, etc., at the Aalto University and Millimetre Wave Laboratory of Finland - ESA External Laboratory (MilliLab): under his supervision 56 students have received the doctor degree. He has authored or coauthored over 500 scientific or technical papers and seven books, e.g., Semiconductor Terahertz Technology: Devices and Systems at Room Temperature Operation (Wiley, 2015).

Dr. Räisänen has been Conference Chairman of several international microwave and millimeter-wave conferences including the 1992 European Microwave Conference and the 2016 Global Symposium on Millimeter Waves. He was an Associate Editor of the IEEE Transactions on Microwave Theory and Techniques (2002–2005). He was a member of the Board of Directors of the European Microwave Association (EuMA) (2006–2011). He has been the Chairman of the Board of Directors of MilliLab since its establishment in 1995.

Dr. Räisänen has been the Edmond S. Gillespie Fellow of the Antenna Measurement Techniques Association (AMTA) since 2008. He was the recipient of the AMTA Distinguished Achievement Award in 2009. The Chair of Excellence by the University Carlos III of Madrid (UC3M) was awarded to him in 2013. He has received two Decorations from the President of the Republic of Finland: Knight First Class of the Order of the White Rose of Finland (2001) and Commander of the Order of the Lion of Finland (2017). In 2017, he received the EuMA Distinguished Service Award and was conferred the Honorary Doctorate of UC3M.

Zachary D. Taylor (S'06–M'09) received the B.S. degree in electrical engineering from the University of California (UCLA), Los Angeles, CA, USA, in 2004, and the M.S. and Ph.D. degrees in electrical engineering from the University of California (UCSB), Santa Barbara, CA, USA, in 2006 and 2009, respectively. From 2013 – 2018 he was an adjunct assistant professor with appointments in the Department of Bioengineering, Department of Electrical Engineering, and Department of Surgery at the University of California (UCLA), Los Angeles, CA, USA. From 2018, he is an assistant professor in the Department of Electronics and Nanoengineering at Aalto University, Espoo, Finland. His current research interests include submillimeter-wave and THz imaging and sensing and THz frequency calibration techniques for antenna measurements, personnel imaging, and clinical diagnostics.